

# Isogeometric Galerkin-characteristic analysis for miscible flows in porous media

Abdelouahed Ouardghi<sup>1</sup>[0000-0003-3471-7424] and Ilham  
Asmouh<sup>2</sup>[0009-0001-9930-9555]

<sup>1</sup> Forschungszentrum Jülich GmbH, Jülich Supercomputing Centre,  
Wilhelm-Johnen-Straße, Jülich, 52428, Germany  
[a.ouardghi@fz-juelich.de](mailto:a.ouardghi@fz-juelich.de)

<sup>2</sup> Institut für Mathematik, Universität Innsbruck, Technikerstraße 13, 6020  
Innsbruck, Austria  
[ilham.asmouh@uibk.ac.at](mailto:ilham.asmouh@uibk.ac.at)

**Abstract.** This note presents a NURBS-based isogeometric analysis (IgA) combined with an  $L^2$ -projection characteristic-Galerkin method to deal with incompressible miscible problems. The advection part is treated in a semi-Lagrangian framework, where high-order non uniform rational B-spline (NURBS) functions are used to interpolate the solution. The resulting semi-discrete equation is solved using an efficient backward differentiation time-stepping algorithm, where Darcy velocity and pressure are updated within each timestep. The accuracy of the method is analyzed through a miscible displacement of an incompressible fluid, where the analytical solution is known, and a real problem with a viscous fingering in porous media. The numerical results presented in this study demonstrate the potential of the proposed IgA characteristic-Galerkin method to allow for large time steps in the computations without deteriorating the accuracy of the obtained solution and to accurately maintain the shape of the solution in the presence of complex patterns in the solution.

**Keywords:** Darcy flow · Incompressible miscible displacement · Convection-Dispersion problems · Characteristic-Galerkin · Isogeometric analysis ·  $L^2$ -projection.

## 1 Introduction

In this note, given a bounded domain  $\Omega \subset \mathbb{R}^d$ ,  $d \in \{1, 2, 3\}$ , with Lipschitz boundary and a given time interval  $[0, T]$ , we propose a novel Isogeometric Modified Method of Characteristics (IgMMC) for the miscible displacement of an incompressible fluid by another in a porous medium, described by the following

time-dependent coupled system of partial differential equations

$$\begin{aligned}
\frac{Dc}{Dt} - \nabla \cdot (\mathcal{D}(\mathbf{u}))\nabla c &= g(c), \quad \text{in } \Omega \times [0, T], \\
c(\mathbf{x}, 0) &= c_0(\mathbf{x}), \quad \text{in } \Omega, \\
-\frac{\mathbf{K}(\mathbf{x})}{\mu(c)}\nabla P &= \mathbf{u}, \quad \text{in } \Omega \times [0, T], \\
\nabla \cdot \mathbf{u} &= f, \quad \text{in } \Omega \times [0, T], \\
P &= P_D, \quad \text{on } \Gamma^D \times [0, T], \\
\mathbf{u} \cdot \mathbf{n} &= u_N, \quad \text{on } \Gamma^N \times [0, T],
\end{aligned} \tag{1}$$

where  $\frac{Dc}{Dt} = \frac{\partial c}{\partial t} + \mathbf{u} \cdot \nabla c$  denotes the material derivative. Our main interest consists of solving the problem above for  $\mathbf{u}(\mathbf{x}, t)$ , which represents the Darcy velocity, i.e., the volume of fluid flowing through a unit section per unit time. We are also interested in finding  $P(\mathbf{x}, t)$ , which represents the Darcy pressure in the fluid mixture, and  $c(\mathbf{x}, t)$  the concentration of the fluid which refers to the amount of species per unit volume of the fluid mixture. The parameter  $\alpha(c) = \frac{\mathbf{K}(\mathbf{x})}{\mu(c)}$  denotes the quotient of the permeability of the porous rock  $\mathbf{K}(\mathbf{x})$  divided by the viscosity of the fluid mixture  $\mu(c)$ ,  $g(c)$  refers to the source term which can be a nonlinear function, and the function  $f$  is the imposed external total flow rate as sum of sources and sinks. The dispersion tensor, denoted as  $\mathcal{D}(\mathbf{u}(\mathbf{x}, t))$ , encapsulates the combined effects of molecular diffusion and mechanical dispersion within a porous medium. Its components are defined as follows:

$$\begin{aligned}
\mathcal{D}_{11} &= d_m + \frac{\alpha_L u^2 + \alpha_T v^2}{\sqrt{u^2 + v^2}}, \quad \mathcal{D}_{12} = \mathcal{D}_{21} = (\alpha_L - \alpha_T) \frac{uv}{\sqrt{u^2 + v^2}}, \\
\mathcal{D}_{22} &= d_m + \frac{\alpha_L v^2 + \alpha_T u^2}{\sqrt{u^2 + v^2}}.
\end{aligned} \tag{2}$$

In this context,  $\mathbf{u}(\mathbf{x}, t) = (u, v)$  represents the local Darcy velocity vector,  $d_m$  is the molecular diffusion coefficient, and  $\alpha_L$  and  $\alpha_T$  are the longitudinal and transverse dispersivity coefficients, respectively. This formulation reflects the anisotropic nature of dispersion in porous media, where solute spreading is influenced by both the direction and magnitude of the flow field. This mathematical model is subject to many tangible applications such as oil recovery, environmental pollution [8], groundwater contamination, petroleum engineering, acoustics and biomechanics. Miscible flows are generally a combination of Darcy's law with the mass transport of the solvent by the advection phenomena and hydrodynamic dispersion phenomena. In the field of oil industry for example, the main challenge consists of existence of fingering instability due to the viscosity and the density difference between the oil and the solvent [6]. This is essentially attributed to the dominance of the advection where Peclet number takes large values. It is well known that the standard Galerkin formulation where Eulerian schemes are adopted produces unstable discretizations, unless the time interval is very refined (CFL stability condition).

In this paper, the convection part is integrated using the IgMMC where the concentration at the next level is updated based on the NURBS functions in the  $L^2$ -projection framework. The dispersion operator is then discretized using IgA and the resulting semi-discrete problem is integrated using a second-order BDF2 scheme. The performance of the proposed IgMMC is demonstrated first for a miscible displacement of an incompressible fluid, described by a time-dependent coupled system of convection-dispersion equations with analytical solution. The study is extended then to a real test case consisting of a viscous fingering in porous media with irregular pores. The numerical results presented in this study demonstrate the potential of the IgMMC to allow for large time steps in the computations without deteriorating the accuracy of the obtained solutions which makes it an attractive choice over the conventional Eulerian-based methods.

## 2 Formulation of the method

### 2.1 Calculation of the departure points

The first step is to compute the departure points. To this end, we are given two knot vectors  $\Xi^1 = (\xi_1, \xi_2, \dots, \xi_{m_b+p+1})$  and  $\Xi^2 = (\eta_1, \eta_2, \dots, \eta_{l_b+q+1})$ , which consist of an ordered set of non-decreasing parameter values, where  $m_b$  and  $l_b$  denote the number of basis functions of degree  $p$  and  $q$  in  $\Xi^1$  and  $\Xi^2$  directions respectively, and  $\xi_i, \eta_i$  represent the knots which partition the parametric domain into  $\tilde{\Omega} = \cup_{k=1}^{N_e} \tilde{\mathcal{P}}_k$ . They are then mapped into a set of physical elements  $\mathcal{P}_k$  as  $\Omega = \cup_{k=1}^{N_e} \mathcal{P}_k$ , with  $N_e$  denotes the total number of elements. It should be stressed that in IgA-based techniques, the space of basis functions is inherited from the space used to parametrize the geometry. Therefore, the elements are represented in the physical domain  $\Omega$  by mapping the mesh to the physical space via the following NURBS geometrical map

$$S : \tilde{\Omega} \longrightarrow \Omega, \quad (\tilde{\xi}, \tilde{\eta}) \longmapsto S(\xi, \eta) = \sum_{m=1}^{\text{nDoF}} \mathcal{R}_m^{p,q}(\xi, \eta) B_m, \quad (3)$$

where  $\tilde{\Omega}$  refers to the parametric space, see Figure 1 for an illustration.  $\mathcal{R}_m^{p,q}$  denotes the compact form of the basis function given by  $\mathcal{R}_m^{p,q}(\xi, \eta) = \mathcal{R}_i^p(\xi) \mathcal{R}_j^q(\eta)$ , where  $\mathcal{R}_i^p(\xi)$ ,  $\mathcal{R}_j^q(\eta)$  denote the NURBS basis functions [4], and  $\text{nDoF} = m_b \times l_b$  is the total number of control points of the vector  $B$ . In addition, we discretize the time interval into sub-intervals  $[t_n, t_{n+1}]$  with length  $\Delta t$ . It should be stressed that the main drawback of NURBS functions consists of the fact that they are not interpolatory. In this study, an  $L^2$ -projection approach is used as remedy to this problem [1]. Therefore, the parent space is provided with a certain number of quadrature points which are then mapped to each element  $\tilde{\mathcal{P}}_k$  in the parametric domain  $\tilde{\Omega}$ . We denote them  $\tilde{\xi}_{k,g} = (\xi_{k,g}, \eta_{k,g})^\top$  with corresponding weights  $\omega_{k,g}$  for  $g = 1, \dots, N_{k,g}$  where  $N_{k,g}$  is the total number of quadrature points in the element  $\tilde{\mathcal{P}}_k$ . The characteristic curves  $\tilde{\mathcal{Y}}(\tau, \tilde{\xi}_{k,g})$  are then calculated for

each quadrature point  $\tilde{\xi}_{k,g}$  in the parametric space by solving the backward differential equations

$$\frac{d\tilde{\mathcal{Y}}(\tau, \tilde{\xi}_{k,g})}{d\tau} = \mathbf{v}(\tilde{\mathcal{Y}}(\tau, \tilde{\xi}_{k,g})), \quad \forall \tau \in [t_n, t_{n+1}], \quad \tilde{\mathcal{Y}}(t_{n+1}, \tilde{\xi}_{k,g}) = \tilde{\xi}_{k,g}, \quad (4)$$

where  $\tilde{\mathcal{Y}}(\tau, \tilde{\xi}_{k,g})$  denotes the departure point defined at time  $\tau$  of a particle that will reach  $\tilde{\xi}_{k,g} = (\tilde{\xi}_{k,g}, \tilde{\eta}_{k,g})^\top$  at time  $t_{n+1}$ . Note that the accuracy of a semi-Lagrangian scheme is related to the accuracy of the scheme used to calculate the departure points. In this work, the well-established fourth-order Runge-Kutta scheme is used and the result is mapped to  $\mathcal{Y}^n(\mathbf{x}_{k,g})$ .

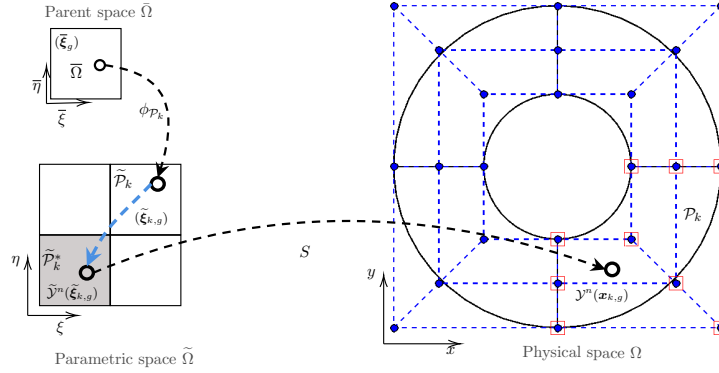


**Fig. 1.** A schematic diagram illustrating the main quantities needed for the computation of the departure points. In a first step, each quadrature point  $\tilde{\xi}_g = (\tilde{\xi}_g, \tilde{\eta}_g)$  is mapped from the parent space to the parametric space according to the mapping  $\phi_{P_k}$ . This results in the point  $\tilde{\xi}_{k,g} = (\tilde{\xi}_{k,g}, \tilde{\eta}_{k,g})$ . The corresponding departure point  $\tilde{\mathcal{Y}}^n(\tilde{\xi}_{k,g})$  is then calculated at the host element, see the dark element  $\tilde{P}_k^*$ , before being mapped to the physical element  $P_k$ . This results in the departure point  $\mathcal{Y}^n(\mathbf{x}_{k,g})$ .

## 2.2 Isogeometric $L^2$ -projection BDF2

The discrete spaces in the physical domain, for the concentration, the pressure and the velocity, are defined as

$$\mathcal{W}_h := \left\{ w_h : w_h \circ S \in \mathcal{N}^{p,q}(\Xi_1^{c_h}, \Xi_2^{c_h}), w_h|_{\partial\Omega} = 0 \right\},$$

$$\mathcal{P}_h := \left\{ q_h : q_h \circ S \in \mathcal{N}^{p-1,q-1}(\Xi_1^{q_h}, \Xi_2^{q_h}) \right\},$$

$$\mathcal{V}_h := \left\{ \mathbf{v}_h : \mathbf{v}_h \circ S \in (\mathcal{N}^{p,q}(\Xi_1^{v_h}, \Xi_2^{v_h}))^2 \right\},$$

where  $\mathcal{N}^{p,q} \equiv \mathcal{N}^{p,q}(\Xi_1, \Xi_2, p, q) := \text{span}\{\mathcal{R}_m^{p,q}\}_{m=1}^{\text{nDoF}}$ , denotes the two dimensional space of NURBS functions of degrees  $(p, q)$  and determined by the tensor product of two knot vectors  $(\Xi_1, \Xi_2)$ . Here, each set  $(\Xi_1^{v_h}, \Xi_2^{v_h})$  has the same knots as the set  $(\Xi_1^{q_h}, \Xi_2^{q_h})$  with a multiplicity increased by one in order to satisfy the same continuity property for both the pressure and the velocity [2]. Recall that at a knot of multiplicity  $m$ , a NURBS function of degree  $p$  is  $\mathcal{C}^{p-m}$  continuous [4]. We are additionally given the set  $\mathcal{V}_h^0 \subset \mathcal{V}_h$  which reads the space of discrete functions that vanish on the boundary of  $\Omega$ . Therefore, the discrete variational form associated to (1) reads: Find an isogeometric Galerkin solution  $(c_h, \mathbf{u}_h, P_h)$  to the exact solution  $(c, \mathbf{u}, P)$  such that

$$\begin{aligned} \left( \frac{\mu(c_h)}{\mathbf{K}(\mathbf{x})} \mathbf{u}_h, \mathbf{v}_h \right) &= (P_h, \nabla \cdot \mathbf{v}_h), \quad \forall \mathbf{v}_h \in \mathcal{V}_h^0, \\ (\nabla \cdot \mathbf{u}_h, q_h) &= (f, q_h), \quad \forall \mathbf{v}_h \in \mathcal{P}_h \\ \left( \frac{Dc_h}{Dt}, w_h \right) - (\mathcal{D}(\mathbf{u}_h) \nabla c_h, \nabla w_h) &= (g(c_h), w_h), \quad \forall \mathbf{v}_h \in \mathcal{W}_h. \end{aligned} \quad (5)$$

Applying the second-order BDF2 scheme, we can rewrite equations (5) in a more compact form as

$$[\mathbf{A}] \{ \mathbf{C}^{n+1} \} = \{ \mathbf{dRhs}^n \}, \quad (6)$$

$$\begin{pmatrix} \mathcal{A}_c & \mathcal{B} \\ \mathcal{B}^T & \mathbf{0} \end{pmatrix} \begin{pmatrix} \mathbf{U}^{n+1} \\ P^{n+1} \end{pmatrix} = \begin{pmatrix} P \mathbf{Rhs}^n \\ u \mathbf{Rhs}^n \end{pmatrix}, \quad (7)$$

where  $[\mathbf{A}] = \left( \frac{3}{2\Delta t} [\mathbf{M}] + [\mathbf{S}] + \mathbf{G}^{n+1} \right)$  is nDoF  $\times$  nDoF-valued matrix and  $\{ \mathbf{dRhs} \} = \left( \frac{2}{\Delta t} \{ \tilde{\mathbf{H}}^n \} - \frac{1}{2\Delta t} \{ \hat{\mathbf{H}}^{n-1} \} \right)$  is nDoF-valued vector, where  $\tilde{\mathbf{H}}^n$  and  $\hat{\mathbf{H}}^{n-1}$  are the  $L^2$ -projection approximation of integrals with the following entries

$$H_m^n := \int_{\Omega} c^n (\mathcal{Y}_{n+1}^n(\mathbf{x})) \mathcal{R}_m^{p,q}(\mathbf{x}) d\Omega, \quad H_m^{n-1} := \int_{\Omega} c^{n-1} (\mathcal{Y}_{n+1}^{n-1}(\mathbf{x})) \mathcal{R}_m^{p,q}(\mathbf{x}) d\Omega. \quad (8)$$

Using Gauss–Legendre quadrature rule, the first integral in (8) is approximated as follows

$$\begin{aligned} \int_{\Omega} c^n (\mathcal{Y}_{n+1}^n(\mathbf{x})) \mathcal{R}_m^{p,q}(\mathbf{x}) d\Omega &= \sum_{k=1}^{N_e} \int_{\Omega} c^n (\mathcal{Y}_{n+1}^n (G_{\mathcal{P}}^{p,q}(\bar{\xi}, \bar{\eta}))) \mathcal{R}_m^{p,q} (G_{\mathcal{P}}^{p,q}(\bar{\xi}, \bar{\eta})) |J(\bar{\xi}, \bar{\eta})| d\bar{\Omega} \\ &\approx \sum_{k=1}^{N_e} \sum_{g=1}^{N_{k,g}} w_{k,g} c^n (\mathcal{Y}_{n+1}^n (G_{\mathcal{P}}^{p,q}(\bar{\xi}_g, \bar{\eta}_g))) \mathcal{R}_m^{p,q} (G_{\mathcal{P}}^{p,q}(\bar{\xi}_g, \bar{\eta}_g)) |J(\bar{\xi}_g, \bar{\eta}_g)| \\ &= \sum_{k=1}^{N_e} \sum_{g=1}^{N_{k,g}} w_{k,g} \tilde{c}_{k,g}^n \mathcal{R}_m^{p,q} (G_{\mathcal{P}}^{p,q}(\bar{\xi}_g, \bar{\eta}_g)) |J(\bar{\xi}_g, \bar{\eta}_g)| = \tilde{H}_m^n, \end{aligned} \quad (9)$$

where,  $\tilde{c}_{k,g}^n = c^n(\mathcal{Y}_{n+1}^n(\mathbf{x}_{k,g}))$  is the solution at the departure point  $\mathcal{Y}_{n+1}^n(\mathbf{x}_{k,g})$  for which the values are calculated as

$$\tilde{c}_{k,g}^n := c^n (\mathcal{Y}_{n+1}^n(\mathbf{x}_{k,g})) \approx \sum_{a=1}^{N_p} c_a^n \mathcal{R}_{p,q}^a (\mathcal{Y}_{n+1}^n(\mathbf{x}_{k,g})), \quad (10)$$

where  $c_a^n$ ,  $a = 1, \dots, N_p$ , denote the known solutions at the control points of element  $\mathcal{P}_k$ , which corresponds to the mapping of the host element  $\tilde{\mathcal{P}}_k^*$  at time  $t_n$  to which the departure point  $\mathcal{Y}_{n+1}^n(\mathbf{x}_{k,g})$  belongs, and  $N_p$  is the total number of control points within the host element  $\mathcal{P}_k$  which is directly related to the used NURBS's degree, see Figure 1 for an illustration. Further note that  $w_{k,g}$  denote the quadrature weights of the Gauss-Legendre quadrature rule used in our study to evaluate the integrals, and  $|J_k(\tilde{\xi}_g, \tilde{\eta}_g)|$  is the determinant of Jacobian of the map  $G$  from the parent space to the element  $\mathcal{P}_k$  in physical space. The mapping  $G_{\mathcal{P}_k} : \bar{\Omega} \rightarrow \mathcal{P}_k$  is given by the composition  $S \circ \phi_{\mathcal{P}}$ , where the function  $\phi_{\mathcal{P}}$  maps the parent space  $[-1, 1] \times [-1, 1]$  to the parametric element  $\tilde{\mathcal{P}} = [\tilde{\xi}_i, \tilde{\xi}_{i+1}] \times [\tilde{\eta}_j, \tilde{\eta}_{j+1}]$ . The integral  $H_m^{n-1}$  is approximated in the same manner as equation (9) where the solution in (10) is evaluated two time steps back along the characteristics using  $\mathcal{Y}_{n+1}^{n-1}(\mathbf{x}_{k,g})$ . The quantities  $\mathcal{A}_c$  and  $\mathcal{B}$  are nDoF  $\times$  nDoF and nDoF  $\times$  Pndof matrices whose elements entries are respectively given by

$$\mathcal{A}_{ml}^n = \int_{\Omega} \alpha(c)^{-1} (\mathcal{R}_l^{p,q}(\mathbf{x}) \cdot \mathcal{R}_m^{p,q}(\mathbf{x})) d\Omega, \quad \mathcal{B}_{ml} = \int_{\Omega} (\nabla \cdot \mathcal{R}_l^{p,q}(\mathbf{x})) \mathcal{R}_m^{p-1,q-1}(\mathbf{x}) d\Omega.$$

The quantity  $\mathcal{R}_l^{p-1,q-1}$  refers to the NURBS basis functions corresponding to the pressure  $P$  with the total number of degrees of freedom Pndof and  $\mathcal{R}_l^{p,q} := (\mathcal{R}_l^{p,q}, \mathcal{R}_l^{p,q})$  are the NURBS basis functions corresponding to the velocity  $\mathbf{u}$  with the total number of degrees of freedom nDoF. The right-hand side vectors  $\{^P \mathbf{RhS}^{n+1}\}$  and  $\{^u \mathbf{RhS}^{n+1}\}$  are with entries

$$\begin{aligned} \{^P \mathbf{RhS}^{n+1}\}_l &= - \int_{\Gamma_D} P_D^{n+1}(\mathbf{x}) (\mathcal{R}_l^{p,q}(\mathbf{x}) \cdot \mathbf{n}(\mathbf{x})) d\Gamma \quad l = 1, 2, \dots, \text{nDoF}, \\ \{^u \mathbf{RhS}^{n+1}\}_m &= - \int_{\Omega} f^{n+1}(\mathbf{x}) \mathcal{R}_m^{p-1,q-1}(\mathbf{x}) d\Omega \quad m = 1, 2, \dots, \text{Pndof}. \end{aligned} \quad (11)$$

The computation of integrals (11) are approximated using Gauss-Legendre quadrature rule. Moreover, the matrix  $\mathcal{A}_c$  consists of the main coupling between the transport-dispersion equation and Darcy equations. A splitting approach is used where the transport-dispersion equation is solved at a first stage and the obtained concentration is inserted in (7) to update the Darcy velocity and pressure. It should be noted that this matrix depends on the concentration and hence should be updated at each timestep.

### 3 Numerical experiments

In this section, we present numerical simulations to assess the performance of our method. We begin with a convection-diffusion problem characterized by a moving front, serving as a benchmark for accuracy and stability. Next, we consider a coupled convection-dispersion system with Darcy flow, where an analytical solution allows for direct validation. Finally, we apply our approach to a more complex scenario, subject to a fingering simulation within an arbitrarily shaped pore structure demonstrating the method's capability in realistic porous media.

#### 3.1 Moving fronts problem

In this example we consider the problem of moving fronts in a squared domain  $\Omega = [0, 1] \times [0, 1]$  governed by the convection-diffusion equations given in (1)

with a time-dependant velocity field  $\mathbf{u} = (u, v)^\top$  defined by

$$u(t, x, y) = \frac{-0.1e^{-\alpha_1(t,x)} + 0.5e^{-\alpha_2(t,x)} + e^{-\alpha_3(t,x)}}{e^{-\alpha_1(t,x)} + e^{-\alpha_2(t,x)} + e^{-\alpha_3(t,x)}},$$

$$v(t, x, y) = \frac{-0.1e^{-\alpha_1(t,y)} + 0.5e^{-\alpha_2(t,y)} + e^{-\alpha_3(t,y)}}{e^{-\alpha_1(t,y)} + e^{-\alpha_2(t,y)} + e^{-\alpha_3(t,y)}},$$

where

$$\alpha_1(t, z) = \frac{0.05}{\nu}(z - 0.5 + 4.95t), \quad \alpha_2(t, z) = \frac{0.25}{\nu}(z - 0.5 + 0.75t), \quad \alpha_3(t, z) = \frac{0.50}{\nu}(z - 0.375),$$

with  $z = x$  or  $y$ . It is also easy to verify that the analytical solution of this problem is given by

$$c(t, x, y) = u(t, x, y)v(t, x, y).$$

This problem has been previously solved in [7] using a moving finite element method and in [5] using a family of finite element alternating-direction methods combined with a modified method of characteristics. Initially, two separate fronts travel along the main diagonal of the computational domain at different speeds and eventually coalesce into one front for longer time. In all simulations for this benchmark, a uniform mesh consisting of  $32 \times 32$  grids of squared patches with patch side length  $h = 1/32$  is considered. Refinements are performed by the  $k$ -refinement method, and the numerical solutions are computed using different NURBS degrees ranging from  $p = 1$  to  $p = 5$ . To examine the convergence behavior of the IgMMC method for this problem, we set the CFL number to  $\text{CFL} = 5$  and we display in Figure 2 the convergence plots of  $L^1$ -error against the number of degrees of freedom using  $p = 1, 2, 3, 4$  and  $5$  for three different values of the diffusion coefficient  $\nu = 4 \times 10^{-3}$ ,  $\nu = 10^{-3}$  and  $\nu = 5 \times 10^{-4}$  at time  $t = 0.2$ . The clear indication from Figure 2 is that the slopes of the convergence plots are consistent with the expected convergence rates of the considered NURBS degrees for this test example. For instance, using  $5 \times 10^{-4}$  the slopes of the convergence plots for linear, quadratic, cubic, quartic and quintic NURBS functions are 1.17, 2.31, 3.07, 4.17 and 5.10, respectively. Similar convergence features have been observed for results not reported here for brevity obtained on the mesh with  $64 \times 64$  patches and at time  $t = 0.4$ .

In Figure 3 we display 20 equi-distributed contourlines of the solution at time  $t = 0.2$  using  $\nu = 4 \times 10^{-3}$ ,  $\nu = 10^{-3}$  and  $\nu = 5 \times 10^{-4}$ . Those corresponding to  $t = 0.4$  are displayed in Figure 4. For comparison reason, the exact solution is also presented along side with these numerical results. The clear indication from Figure 3 is that the results obtained using linear, quadratic and cubic degrees are all acceptable for large values of  $\nu = 4 \times 10^{-3}$  and only small distortions are observed in the results obtained using linear and quadratic solutions (observe these results in Figure 3). At the moderate diffusion coefficient  $\nu = 10^{-3}$ , it can be noticed from Figure 3 that linear solution exhibits some oscillations near the proximity of large gradients. These oscillations are corrected by elevating the degree to  $p = 2$ , thus the quadratic and cubic solutions are in good agreement

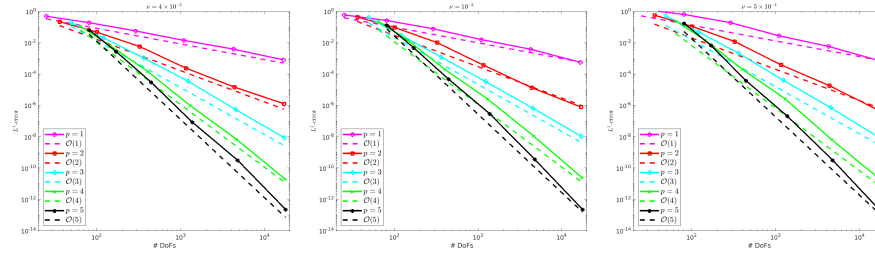


**Fig. 2.** Convergence plots in the  $L^1$ -error for the problem of moving fronts on a mesh with  $32 \times 32$  patches at time  $t = 0.2$  with  $\nu = 4 \times 10^{-3}$  (left),  $\nu = 10^{-3}$  (middle) and  $\nu = 5 \times 10^{-4}$  (right) using different NURBS degrees.

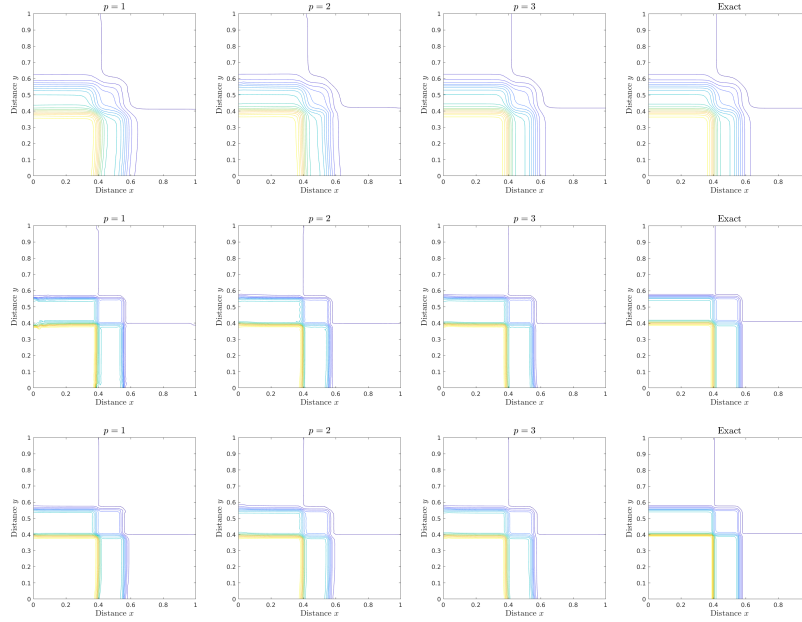


**Fig. 3.** Contourlines of solutions obtained for the problem of moving fronts on a mesh with  $32 \times 32$  patches at time  $t = 0.2$  with  $\nu = 4 \times 10^{-3}$  (first row),  $\nu = 10^{-3}$  (second row) and  $\nu = 5 \times 10^{-4}$  (third row) using different meshes and NURBS degrees. Here,  $p = 1$  (first column),  $p = 2$  (second column),  $p = 3$  (third column) and exact solution (fourth column).

with the exact solution. At the small diffusion coefficient  $\nu = 5 \times 10^{-4}$  corresponding to a convection-dominated problem, less accuracy is observed in the zones where the computed fronts merge. Consequently, the accuracy of the numerical results is reduced for such values of the diffusion coefficient using  $p = 1$  and  $p = 2$ . However, using  $p = 3$  results in precise and accurate results for this

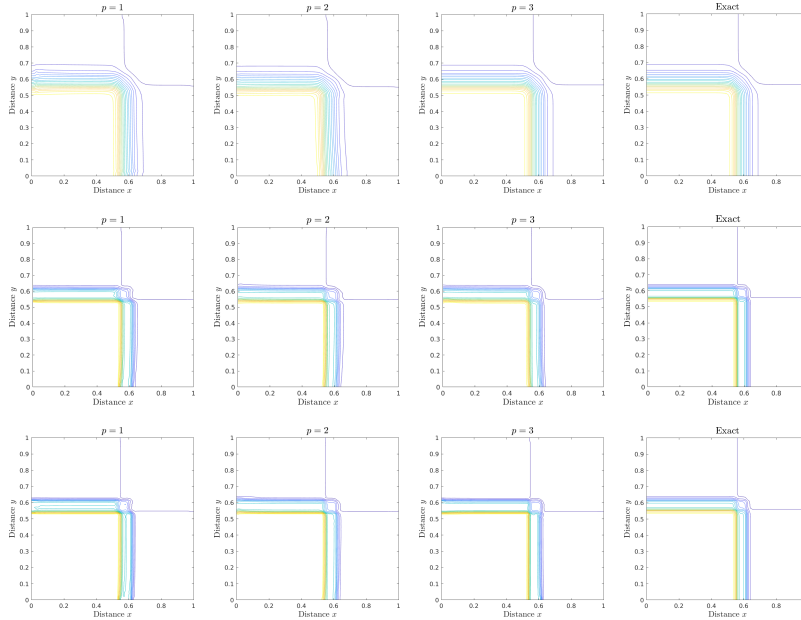
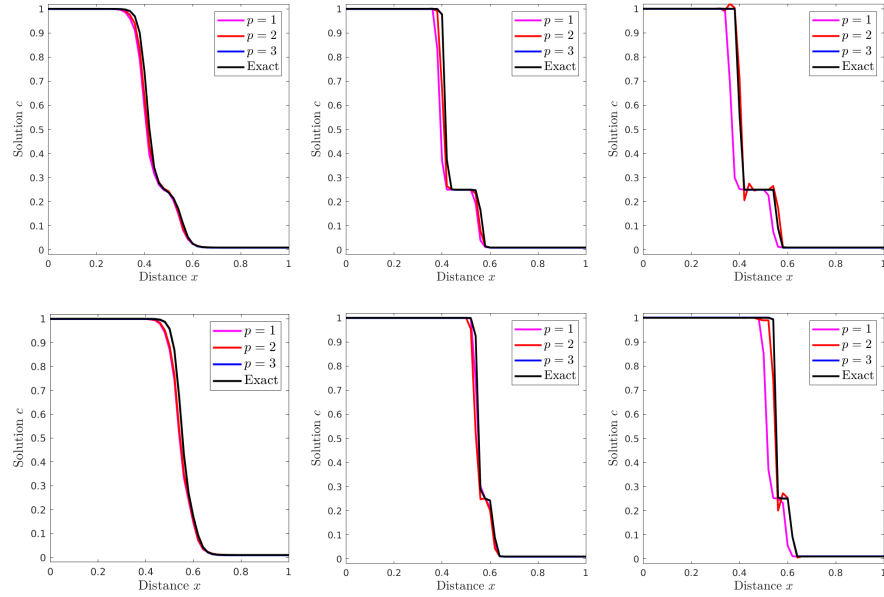


Fig. 4. Same as in Figure 3 but at time  $t = 0.4$ .

test example. Thus, the cubic NURBS degrees are largely enough to capture the sharp gradients in the solutions and produce satisfactory results. The same features can be concluded from the results displayed in Figure 4 which correspond to time  $t = 0.4$ . To further highlight effects of the  $k$ -refinement on the numerical solutions for this example, we present in Figure 5 the corresponding one-dimensional cross-sections at the main diagonal  $y = x$ . Again for the smooth case which corresponds to  $\nu = 4 \times 10^{-3}$ , the selected NURBS degrees produce acceptable results and very small distortion is manifested at the proximity of large gradients. This distortion becomes larger when advancing in time (compare the results in Figure 5). However, using  $\nu = 10^{-3}$ , the numerical dissipation becomes visible in the linear and quadratic solutions and the shock location is shifted compared to the exact solution. This feature is also observed when using  $\nu = 5 \times 10^{-4}$  and oscillations are clearly observed in the quadratic solution at both times  $t = 0.2$  and  $t = 0.4$ . Furthermore, the cubic solution produces very satisfactory results and converges to the exact solution even when highly convective situations are considered. It is to be noted that, the IgMMC method is typically designed to solve this class of convection-dominated problems using time steps ten to twenty times larger than its Eulerian counterparts.



**Fig. 5.** Cross-sections at the main diagonal  $x = y$  of solutions obtained for the problem of moving fronts on a mesh with  $32 \times 32$  patches at time  $t = 0.2$  (first row) and  $t = 0.4$  (second row) with  $\nu = 4 \times 10^{-3}$  (first row),  $\nu = 10^{-3}$  (second row) and  $\nu = 5 \times 10^{-4}$  (third row) using different meshes and NURBS degrees.

### 3.2 Coupled convection-dispersion with Darcy flow

Our prominence in the first example is addressed to test the accuracy of the IgMMC for a miscible flow given by problem (1) over the the domain  $\Omega = [0, 1] \times [0, 1]$ . The analytical solution given by

$$c(x, y, t) = t^2[x^2(x-1)^2 + y^2(y-1)^2],$$

$$\mathbf{u}(x, y, t) = 2t^2 \begin{pmatrix} x(x-1)(2x-1) \\ y(y-1)(2y-1) \end{pmatrix},$$

$$P(x, y, t) = -\frac{1}{2}c^2 - 2c + \frac{17}{6300}t^4 + \frac{2}{15}t^2.$$

The parameters are chosen such that  $T = 0.6$   $\alpha(c) = (c+2)^{-1}$ . The source terms  $f$  and  $g$  are chosen accordingly such as the analytical solutions above are satisfied. The dispersion tensor here is isotropic with  $d_m = 0.02$ ,  $\alpha_L = \alpha_T = 1$ . Therefore  $\mathcal{D}(\mathbf{u}) = (0.02 + |\mathbf{u}|) \mathbf{I}_2$ , where  $\mathbf{I}_2$  is the  $2 \times 2$  identity matrix. The domain is partitioned into quadrilaterals constructed by the cross-product of two one-dimensional NURBS functions with element side length  $h$ . The refinements are performed using the  $k$ -refinement technique to satisfy high inter-element continuity. In Figure 6, we report the convergence plots of the relative  $L^2$ -errors of

the concentration  $c$ , the Darcy velocity  $u$ -component and the Darcy pressure  $P$ , at time  $t = 0.6$ . Here, the errors are plotted against the meshsize  $h$ . Consistently with previous observations in [9, 3], the present IgMMC provides a high-order accuracy of the miscible displacement demonstrated by  $\mathcal{O}(p)$  for the concentration and the pressure, and by  $\mathcal{O}(p - \beta)$  for the velocity, where  $\beta$  is ranging from 0.02 and 0.37. It is interesting to observe that an accuracy of about  $10^{-4}$  is obtained using  $h = 0.03$  for a NURBS degree  $p = 4$ , however, the NURBS degree  $p = 3$  does not exceed an accuracy of about  $2 \cdot 10^{-4}$  using  $h = 0.015$ . This means that the NURBS mesh used for  $p = 3$  must be refined at least twice in order to achieve the same accuracy obtained for  $p = 4$ . However,  $h$ -refinement may not be the optimal choice as it can lead to dissipation errors in the solution. The reason is that the traditional  $h$ -refinement decreases the inter-element continuity as the number of continuous derivatives decreases by  $m$  if a knot is repeated  $m$  times, see [4] for instance. The highly efficient  $k$ -refinement strategy by its turn, provides smoother functions than the usual Lagrange basis functions, which leads to accurate solutions. It should also be noted that the accuracy of the method is on the same wavelength eventhough a slightly large CFL number is used (CFL = 4.4). Indeed, in contrast to explicit Eulerian advection schemes, the maximum timestep allowed in semi-Lagrangian schemes is not limited to the maximum fluid speed. consequently, it is possible to stably integrate with Courant number that far exceed unity without damaging the accuracy of the solution.

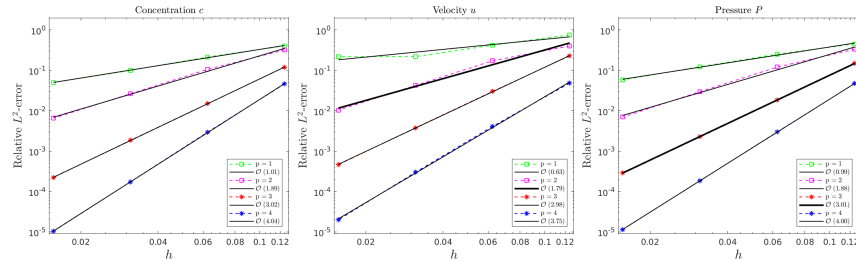


**Fig. 6.** Convergence plots in the relative  $L^2$ -error for Example 3.2 at time  $t = 0.6$ , for  $CFL = 4.4$  and using different NURBS degrees.

### 3.3 Arbitrary shaped pore-scale structure

Having addressed the accuracy of the IgMMC using an academic test with an analytical solution, we consider a more complex structure to demonstrate the capacity of the method. This test case focuses on simulating the miscible flow problem (1) to investigate solute transport through a realistic and more complex pore-scale structure. The setup shown in the left side of Figure 7 is inspired by the one used in [10].

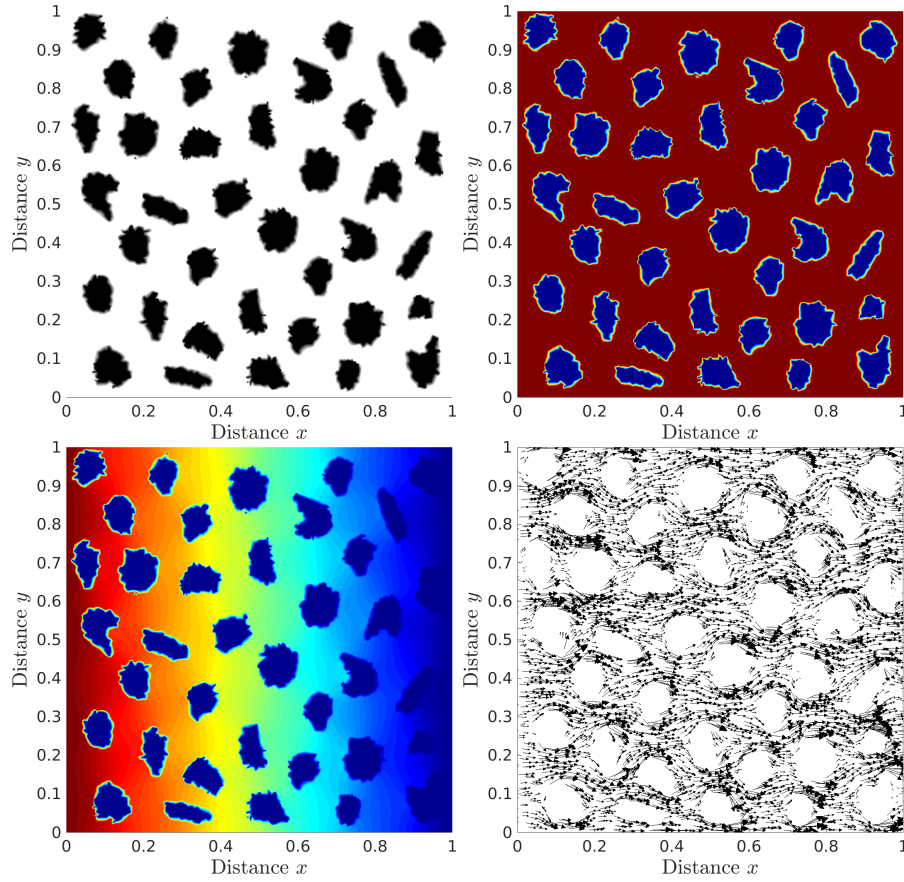


**Fig. 7.** Permeability heterogeneity (first row left), permeability (first row right), the pressure (second row left) and the velocity (second row right) at time  $t = 0.6$ .

The setup allows for in-depth investigation of critical transport phenomena such as the formation of fingering patterns due to viscosity variations, solute mixing induced by flow heterogeneity, and solute dispersion across the domain. In a first simulation, the parameters in the dispersion tensor are fixed in  $\alpha_L = 8 \times 10^{-3}$  and  $\alpha_T = 8 \times 10^{-4}$  and we present the snapshots at different times as shown in Figure 8. The clear indication from this figure is that the simulation demonstrates a high-resolution capture of fluid particle movement through complex pore geometries, where the coupling between transport-dispersion and the Darcy flow equations is handled robustly effectively and the interplay between advection, dispersion, and porous media resistance is well resolved.

Our next objective is to observe the effect of viscosity. To this end, we consider two cases with low and high viscosity values where initially, the flow is dominated by transversal viscosity, leading to limited cross-channel mixing. Later,

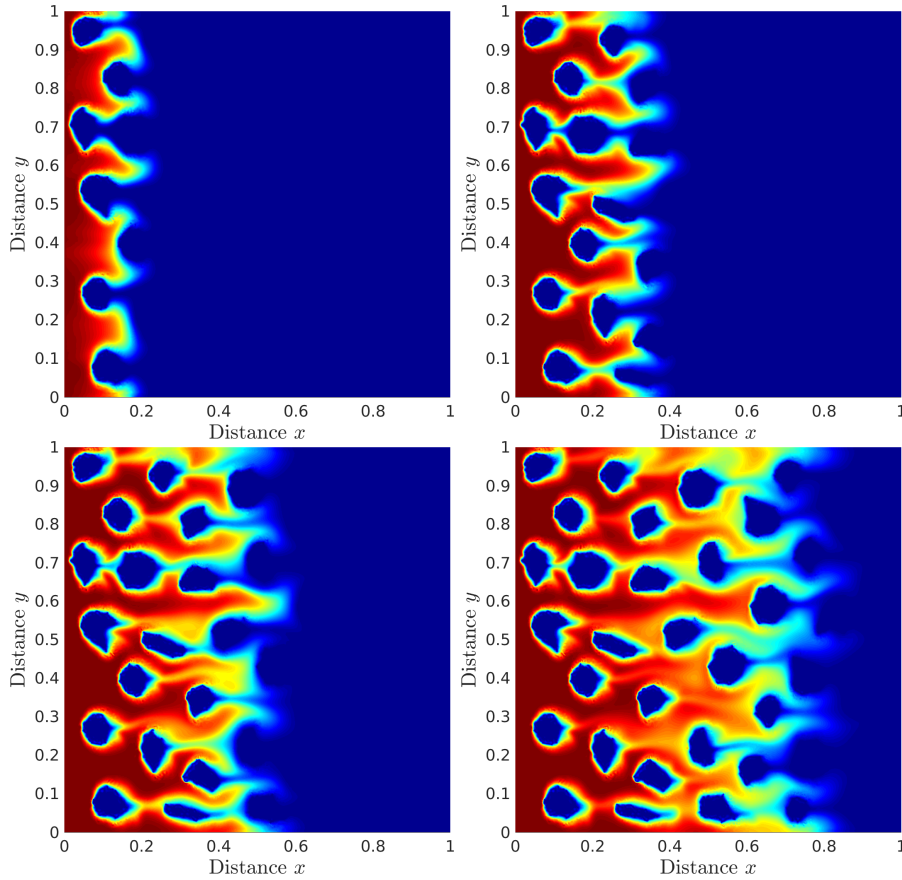


**Fig. 8.** Snapshot of the miscible displacement process at times  $t = 0.15$ ,  $t = 0.30$  (first row), and at times  $t = 0.45$ , and  $t = 0.60$  (second row).

the longitudinal viscosity becomes dominant, redirecting the flow and enhancing longitudinal dispersion. By comparing the low and high viscosity cases, the simulations clearly reveal the impact of viscosity on flow channelization. In the higher viscosity scenario, the flow becomes smoother and more damped, reducing the sharpness of mixing fronts and delaying breakthrough (observe the right column of Figure 9). On the other hand, by comparing the two rows of the same figure, it is clear that increased transverse viscosity components lead to broader dispersion across flow streamlines, enhancing transverse mixing, whereas high longitudinal viscosity suppresses sharp advective fronts, promoting more diffusive transport. It is worth to say that despite the complexity introduced by the full viscosity tensor, the presented IgMMC remains stable and accurate, effectively capturing the coupled transport-flow interaction and resolving anisotropic diffusion mechanisms across the pore domain.

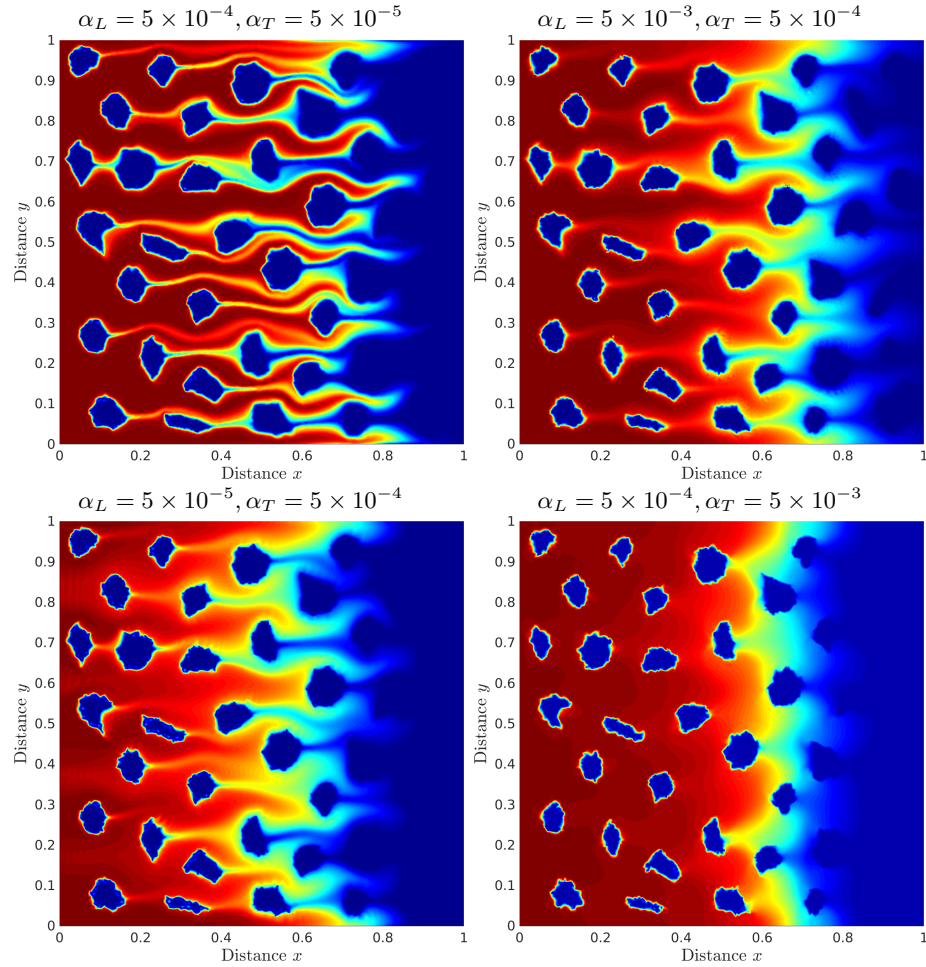


**Fig. 9.** Effects of viscosity on the miscible displacement process in the porous medium.

## Conclusions

In this letter we have presented a IgMMC for solving a class of incompressible miscible displacements, which consist of coupled convection-dispersion equations and Darcy flow. These problems generate a variety of challenging and pose severe constraints to the creation of the computational grids, since their geometry may give rise to distorted and badly shaped grid elements. This challenge is dealt with the virtue of IgA as it is recognized as one of the best approach to exactly represent a geometrical object. Another main challenge within these problems is the convection-dominance, especially if the dispersion-tensor depends on the velocity flow. The grid orientation effects are minimized using the characteristic-Galerkin scheme, where the NURBS functions together with an  $L^2$ -projection

approach are used to update the solution during the advection stage. The dispersion term is discretized using IgA, and the resulting semi-discrete problem is solved using a BDF2 scheme. The possibility to use relatively large time steps while keeping the stability all over the method, in response to capturing the multi-scale behaviors, was the main reason behind the BDF2 technique in this paper. By the virtue of the combined techniques, our objective was to minimize the complexity resulting from the multiphysical nature of the whole system. The computed results support our expectations for a stable and highly accurate method for incompressible miscible displacement in porous media.

## References

1. Asmouh, I., El-Amrani, M., Seaid, M.: Isogeometric semi-lagrangian analysis for transport problems. *Applied Mathematics Letters* **130**, 107994 (2022)
2. Hosseini, B., Möller, M., Turek, S.: Isogeometric analysis of the Navier–Stokes equations with Taylor–Hood B-spline elements. *Applied Mathematics and Computation* **267**, 264–281 (2015)
3. Hu, H., Fu, Y., Zhou, J.: Numerical solution of a miscible displacement problem with dispersion term using a two-grid mixed finite element approach. *Numerical Algorithms* **81**, 879–914 (2019)
4. Hughes, T., Cottrell, J., Bazilevs, Y.: Isogeometric analysis: CAD, finite elements, NURBS, exact geometry and mesh refinement. *Computer Methods in Applied Mechanics and Engineering* **194**(39-41), 4135–4195 (2005)
5. Krishnamachari, S., Hayes, L., Russell, T.: A finite element alternating-direction method combined with a modified method of characteristics for convection-diffusion problems. *SIAM Journal on Numerical Analysis* **26**(6), 1462–1473 (1989)
6. Meng, X., Guo, Z.: Localized lattice boltzmann equation model for simulating miscible viscous displacement in porous media. *International Journal of Heat and Mass Transfer* **100**, 767–778 (2016)
7. Mueller, A.: Continuously deforming finite element methods for transport problems. PhD dissertation, University of Texas at Austin (1984)
8. Russell, T.F., Wheeler, M.F.: Finite element and finite difference methods for continuous flows in porous media. In: *The mathematics of reservoir simulation*, pp. 35–106. SIAM (1983)
9. da Veiga, L.B., Pichler, A., Vacca, G.: A virtual element method for the miscible displacement of incompressible fluids in porous media. *Computer Methods in Applied Mechanics and Engineering* **375**, 113649 (2021)
10. Xia, M.: Pore-scale simulation of miscible displacement in porous media using the lattice boltzmann method. *Computers & Geosciences* **88**, 30–40 (2016)